ACIN

High-speed scanning chromatic confocal sensor for 3-D imaging with modeling-free learning control

SHINGO ITO,[1,*] MATHIAS POIK,[1] ERNST CSENCSICS,[1] JOHANNES SCHLARP,[1] AND GEORG SCHITTER[1]

[1]*Christian Doppler Laboratory for Precision Engineering for Automated In-Line Metrology, Automation and Control Institute (ACIN), TU Wien, Vienna, A-1040, Austria*

[*]ito@acin.tuwien.ac.at

Abstract: This paper presents a scanning system that integrates a chromatic confocal displacement sensor for topography measurement of a surface. To take an advantage of its compactness and reliability, an off-the-shelf chromatic confocal displacement sensor is integrated. Instead of moving the sensor, a galvanometer scanner reflects the optical point to increase the scan speed, and fast and accurate scanning motion is realized by learning without a model. The resulting images are corrected based on a geometric model to compensate for image distortion.

© 2020 Optical Society of America

1. Introduction

The surface condition of components and tools influences the quality of the produced goods. For example, the surface roughness of horn antennas varies the transmission of signals [1]. The grain topography of diamond cutting tools influences the cutting performances. Thus, it is desired to acquire 3-D surface images for the improvement of the resulting goods' quality [2]. Especially when the surface condition is monitored directly in the production lines, for example in inline metrology [3], a compact imaging system is indispensable with a sufficiently high imaging resolution and frame rate for the high throughput of the production.

For surface characterization with high accuracy and resolution, high-precision optical displacement sensors can be used to acquire 3-D surface images. An advantage of those sensors is that surfaces can be inspected without contact in order to prevent damage, unlike stylus profilers for example [4]. Among different types of optical methods, laser triangulation has been used to measure surface topography, achieving high accuracy and resolution [5, 6]. A monochromatic confocal displacement sensor enables to inspect the surface topography and also the thickness of transparent layers [7]. However, the focal point of the beam needs to scan perpendicular to the sample (e.g. by a varifocal lens), which increases the complexity of the measurement system [8]. Chromatic confocal displacement sensors solve this problem by using chromatic aberration and are able to simultaneously acquire topography and thickness information without the perpendicular scanning motion [9].

For 3-D imaging with a chromatic confocal displacement sensor, multiple optical points can be created on the target surface, for example by using pin hole arrays. A problem is that a certain distance is required between the optical points to avoid measurement cross-talk [10]. Thus, scanning the optical points is required for high imaging resolution without dead zones. This is typically realized by moving the pin hole arrays optically or mechanically [10–12]. Another challenge is that the light cannot be efficiently used because it is partially blocked by the pin hole array for the emitter [10, 12]. As a result, a high-power light source is required, or a longer measurement time is needed for a sufficient signal-to-noise ratio [10].

A single point chromatic confocal displacement sensor uses the light efficiently. When a single point chromatic confocal displacement sensor is used for 3-D imaging, the sensor head or the

sample is usually laterally scanned by a linear stage or robot [13, 14]. The configuration enables to use a well-developed off-the-shelf chromatic confocal displacement sensor that is compact and calibrated well for inline metrology. However, the scanning speed and the frame rate of the images are limited. This is because the linear stage can be relatively bulky and heavy with low-frequency mechanical resonances that restrict the stage's control bandwidth [15]. Another concern particularly to move the sensor is the slippage of its components (e.g. lenses) due to the acceleration force of the scanning motion. Consequently, the scanning speed is relatively slow with a long imaging time.

This paper proposes a 3-D imaging system where the optical path of a single point chromatic confocal sensor is moved by a scanning mirror, instead of moving the sample or the sensor. Thus, the scanning speed can be significantly increased in comparison with the conventional configuration. Another difference from the conventional configuration is that the light is not always perpendicular to the sample, dependent on the position of the optical point. Thus, its influence on the resulting images is investigated, and highly accurate fast optical scanning is realized by the scanning mirror and modeling-free learning control in this paper. As a feasibility study in this paper, the proposed scanning configuration is applied to the fast lateral scanning axis only while the sample is moved along the slow lateral scanning axis in the conventional way for simplicity.

The paper is organized as follows. Section 2 describes the experimental setup, which is analyzed in Section 3. The algorithm for the learning is introduced and validated for the scanning mirror in Section 4. Section 5 presents model-based image correction by considering the incident angle of the light. The proposed system is demonstrated in Section 6. Section 7 concludes the paper.

2. Hardware architecture

As discussed in Section 1, conventional systems usually carry a chromatic confocal displacement sensor, or a sample is moved, as shown in Fig. 1(a). However, the scanning speed is limited due to the size and weight and for the protection of the sensor. To avoid these problems for a faster scanning speed, the optical path is scanned without moving the sensor and sample in this paper, as shown in Fig. 1(b).
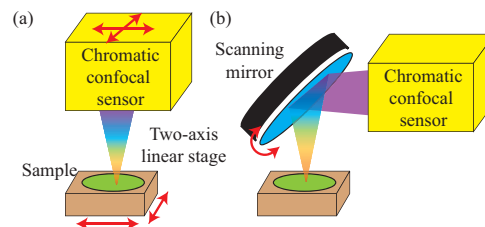

Fig. 1. Scanning system with a chromatic confocal displacement sensor that is implemented by (a) moving the sample or the sensor head and (b) by a scanning mirror. The red arrows indicate the linear and angular motions of the components.

The proposed scanning system is implemented, as shown in Fig. 2(a)(b). A galvanometer scanner (6870M, Cambridge Technology, Bedford, USA) rotates a mirror (6M8715Y-S, Cambridge Technology), which has a dimension of 39.3 mm×24.9 mm×3.2 mm with a silver coating. The mirror redirects the optical beam of a chromatic confocal displacement sensor (IFS2405-30, Micro-Epsilon, Ortenburg, Germany) along the lateral x axis. The confocal sensor head can be

tilted up to ±9° with respect to the sample and has a measurement resolution of 180 nm and an accuracy of 7.5 μm. The acceleration of the head must be less than 2 g (=19.6 m/s^2).

In the case of the scanning along the y axis, a linear stage with a DC motor (VT80, PI, Auburn, USA) moves a sample that is placed on a manual z stage. For bidirectional raster scan, the reference trajectory of the galvanometer scanner is a triangular wave, and that of the linear stage is a ramp signal at a constant velocity. The galvanometer scanner is driven by a current amplifier and connected to an FPGA of a rapid prototyping control system (DS5203, dSpace, Paderborn, Germany), where motion control is implemented for the galvanometer scanner at a sampling frequency of 100 kHz.

The confocal sensor utilizes chromatic aberration such that the focal point of the light along the vertical z axis depends on the wavelength. Thus, the distance can be measured by identifying the wavelength of the lights that are focused on the sample. For this purpose, a spectrometer with a charge coupled device (CCD) is used with an LED in the control unit (IFC2471LED, Micro-Epsilon) of the confocal sensor.

The control unit is used also as a data acquisition system for imaging, recording the measured distance at a sampling rate of 50 kHz. For image correction in Section 5, the FPGA transmits the measured mirror angle θ_x by means of A/B pulse trains [16] at 1 MHz to the control unit, where θ_x is synchronously recorded in addition.

The measured mirror angle and displacement data are stored in the control unit for a set of images. The buffered data are then transmitted to a computer, where 3-D images are reconstructed. Connected also to the servo controller of the linear stage and the rapid prototyping control system via its CPU (DS1005, dSpace), the computer also generates the scanning motion trajectories and regulates the entire system. The width of the setup including the aluminum profiles (see Fig. 2(a)) is approximately 600 mm for the feasibility study.

3. System analysis

3.1. Chromatic confocal displacement sensor

Unlike the conventional scanning configurations in Fig. 1(a), the galvanometer scanner of the proposed scanning system results in an incident angle of the light even if the sample is flat and leveled off. To investigate the influence of the galvanometer scanner's mirror angle θ_x, the exposure time of the CCD to reach the 10 % intensity for a sufficient signal-to-noise ratio is measured with different θ_x and different samples. They are a mirror, an unprocessed silicon wafer, a transparent glass slide (Menzel Glaser, Braunscheig, Germany), and a plastic block (Lego, Billund, Denmark), as shown in Fig. 3. For the experiments, another controller unit (IFC2451, Micro-Epsilon) is used due to availability. The mirror angle θ_x of the galvanometer scanner is defined as 0 when the light is perpendicular to a sample that is leveled off.

The results are shown in Fig. 4, where the exposure time is normalized by the value at $\theta_x = 0$. The results show that a long exposure time is required when the mirror angle is large. This is because an increasing incident angle decreases the light reflected back from the sample to the confocal sensor [9]. Particularly at 4.5°, which corresponds to the maximum tilt angle of the sensor head, an approximately 15 times longer exposure time is required for the reflective mirror and the silicon wafer, while it is only approximately 5 times longer for the plastic block. The reduction is explained by the stronger diffuse reflection of the plastic block, by which more light is reflected back to the confocal sensor [17]. Note that the block is orange as a case study, and the result may depend on the color.

Since a longer exposure time results in a longer measurement time of an image, the proposed scanning configuration has a trade-off between the lateral (x axis) measurement range and the measurement time. For relatively fast imaging, the scanning range of the galvanometer scanner is set to ±2° in the trajectory design of Sec. 4.

The lateral imaging resolution is limited by the diameter of the focused beam spot d_b at $\theta_x = 0$,
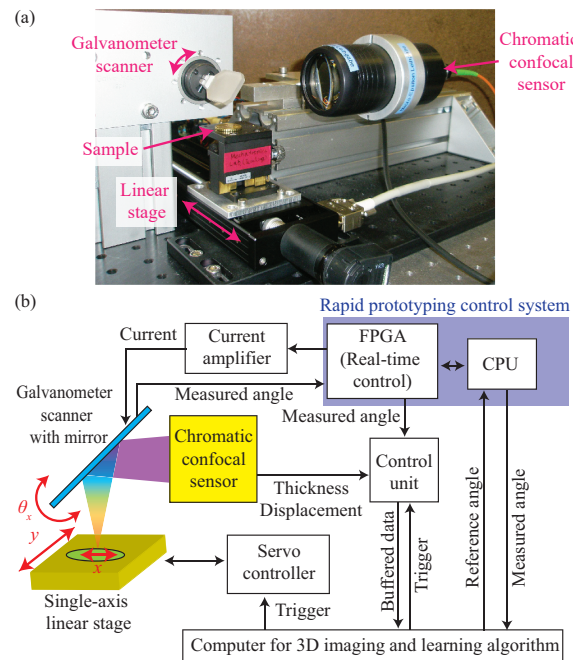
Fig. 2. Proposed scanning chromatic confocal sensor system: (a) photograph and (b) system architecture.
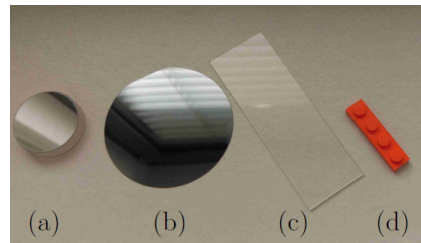

Fig. 3. Photographs of the samples to measure the CCD's exposure time: (a) mirror, (b) unprocessed silicon wafer, (c) glass slide, (d) plastic block.

which is $50\,\mu$m. When the mirror rotates, the focused spot is an ellipse. Its longer diameter increases the lateral resolution to $d_b/\cos 2\theta_x$. This also influences the spectrum of the light to the spectrometer and the distance measurement resolution of the confocal sensor. However, at the maximum scanning angle of $\pm 2°$ for imaging, the longer diameter is $50.1\,\mu$m, which is close to d_b due to the small-angle approximation.
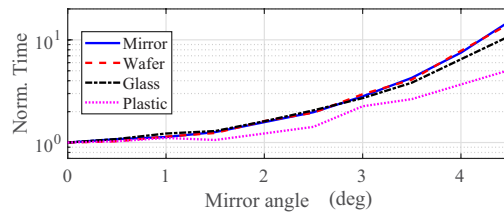
Fig. 4. Normalized exposure time of the CCD to reach its $10\,\%$ light intensity by varying the mirror angle θ_x. The photograph of the samples are shown in Fig. 3.

3.2. Galvanometer scanner

Galvanometer scanners rotate a shaft with a mirror typically up to tens of degrees. Certain types of galvanometer scanners support the shaft by bearings that restrict the lifetime [18]. On the shaft, an angular sensor is mounted to measure the mirror angle [18, 19]. The sensor is usually used for feedback control to regulate the mirror angle. This prevents the mirror angle from drifting during scanning even if the bearing friction is nonlinear and uneven over the motion range.

For fast imaging with uniform resolution, the galvanometer scanner needs to rotate its shaft with the mirror by tracking the trajectory accurately. For the accurate tracking, the feedback controller in Fig. 5 may be designed to maximize the closed-loop control bandwidth. However, such a design degrades the resolution of the mirror motion because the feedback controller strongly feeds sensor noise back to the scanner. In order to avoid this problem for high precision scanning motion, a PID controller is selected as the feedback controller for simplicity and designed such that the closed-loop control bandwidth is minimized to prevent motion drift only during scanning (cf. [20]).
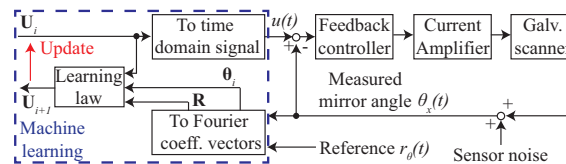

Fig. 5. Control block diagram of the galvanometer scanner.

For the validation of the control design, a complementary sensitivity function, which is the frequency response from the input u to the angle θ_x in Fig. 5, is measured by a network analyzer (3562A, Keysight, Santa Rosa, USA). This measurement is repeated by varying the amplitude of the sine sweep input, as shown in Fig. 6. The magnitude is $0\,\mathrm{dB}$ below $20\,\mathrm{Hz}$, where the PID controller has a sufficiently high gain to compensate for the bearing friction and thermal drift, such that the galvanometer scanner accurately tracks its reference trajectory. However, the magnitude decreases below $-20\,\mathrm{dB}$ between $20\,\mathrm{Hz}$ and $100\,\mathrm{Hz}$ dependent on the input amplitude. This is due to nonlinearity such as static friction [21] that dominates the response with a small input amplitude. The frequency response uncertainties at the low frequencies restrict the lower bound of the achievable closed-loop control bandwidth that is $110\,\mathrm{Hz}$ in this article. The nonlinearity is not visible above $200\,\mathrm{Hz}$, where the magnitude has a slope of $-40\,\mathrm{dB/dec}$, because the inertia of the galvanometer scanner dominates the dynamics.

The frequency response uncertainties and the dynamics of the inertia in Fig. 6 are problematic

for the accurate tracking motion. To overcome them, learning control is utilized in the next section.
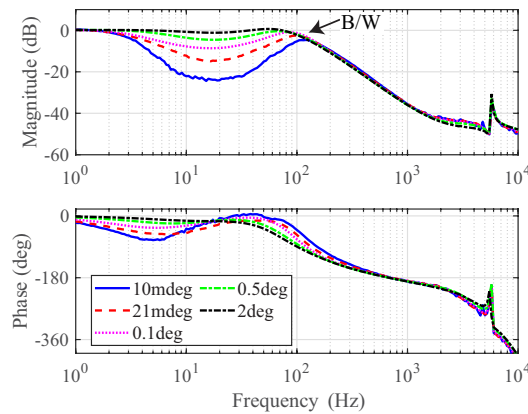

Fig. 6. Measured complementary sensitivity function $T(s)$ when the amplitude of the input sine wave as $u(t)$ is varied between 10 mdeg and 2 deg. The arrow indicates the -3 dB bandwidth at 110 Hz.

4. Modeling-free learning control

Although the low-bandwidth feedback controller of the galvanometer scanner is beneficial for high-precision motion, it cannot compensate for the noninearity and the inertia dynamics for accurate tracking motion. Even in the case of a standard feedback controller, the finite closed-loop bandwidth results in a tracking error for high-speed scanning, and the control input to the galvanometer scanner needs to be accurately adjusted [22]. This process is time consuming, and it is desired to be automated.

To automatically adjust the input u for highly precise and accurate motion, modeling-free inversion-based iterative control (MF-IIC) [23, 24] is utilized as a learning algorithm for the galvanometer scanner. MF-IIC learns from the measured tracking error $e_x = r_\theta - \theta_x$ and updates the input u in the frequency domain such that e_x decreases in the next trial.

As shown in Fig. 5, the trajectory of θ_x is measured and converted to the frequency domain. Based on the frequency-domain angle $\boldsymbol{\theta}$ and the frequency-domain reference $\mathbf{R}$, the learning law finds an input signal $\mathbf{U}$ for the next trial, which is then converted to the time domain.

An advantage of MF-IIC is that it simultaneously carries out system identification (i.e. data driven). An accurate model is unnecessary unlike typical feedforward control [25] and iterative learning control [20, 26]. Due to the internal system identification, MF-IIC can handle the variation of system dynamics [27]. The system identification results can be available in the form of a Jacobian matrix (see (8)). This is beneficial for system analysis, unlike certain algorithms such as artificial neural network, which is difficult for users to interpret [28].

Another advantage of MF-IIC is that the learning action can be activated at the required frequencies only. In the case of periodic scanning motions, they contain the frequency components only at the fundamental and harmonic frequencies. By learning at these frequencies only, MF-IIC filters the sensor noise between the harmonic frequencies for the highly precise and accurate tracking motion [29]. In the following sections, MF-IIC is designed and validated with the galvanometer scanner for high-speed scanning.

4.1. Design of learning control

Among different types of trajectories [30], a band-limited triangular wave is used as the motion reference r_θ for bidirectional imaging with relatively uniform imaging resolution. It is given in the form of Fourier series:

$$r_\theta(t) = \sum_{k=1}^{q_r} (r_k e^{j2\pi k f_r t} + r_k^* e^{-j2\pi k f_r t}), \tag{1}$$

where t, r_k, and r_k^* are the time, the complex Fourier coefficient at the k-th harmonic frequency, and its complex conjugate, respectively. For a high-speed scanning motion, the fundamental frequency f_r is set to 125 Hz with the highest harmonic $q_r = 7$.

For MF-IIC, the Fourier coefficients are represented in the form of a vector $\mathbf{R}$. Similarly, the input u and the measured angle θ_x are also given by vectors

$$\mathbf{R} = [r_1 \dots r_k \dots r_q]^T, \quad \text{where } r_k = 0 \text{ for } k > q_r, \tag{2}$$

$$\mathbf{U} = [u_1 \dots u_k \dots u_q]^T, \tag{3}$$

$$\boldsymbol{\theta} = [\theta_1 \dots \theta_k \dots \theta_q]^T, \tag{4}$$

where u_k and θ_k are the complex Fourier coefficients of $u(t)$ and $\theta_x(t)$ at the k-th harmonic, respectively. The highest learning harmonic q is set to 11, which is higher than q_r, because the friction nonlinearity deforms the scanning trajectory and creates frequency components higher than q_r.

During learning via trials, $\boldsymbol{\theta}$ usually gradually varies, and its derivative with respect to the trial number i is given by

$$\frac{\mathrm{d}\boldsymbol{\theta}_i}{\mathrm{d}i} = \frac{\partial \boldsymbol{\theta}_i}{\partial \mathbf{U_i}} \frac{\mathrm{d}\mathbf{U}_i}{\mathrm{d}i} = \mathbf{J}_i \frac{\mathrm{d}\mathbf{U}_i}{\mathrm{d}i}, \tag{5}$$

where $\mathbf{J}_i$ is the Jacobean matrix at i. The discrete form of the above equation is

$$\boldsymbol{\theta}_{i+1} - \boldsymbol{\theta}_i = \mathbf{J}_i(\mathbf{U}_{i+1} - \mathbf{U}_i). \tag{6}$$

The goal of the learning algorithm is to find the input $\mathbf{U}$ such that the galvanometer scanner tracks its trajectory (i.e. $\boldsymbol{\theta}=\mathbf{R}$). For this purpose, $\boldsymbol{\theta}_{i+1}$ is replaced by $\mathbf{R}$ to rewrite (6) for the learning law of MF-IIC:

$$\mathbf{U}_{i+1} = \mathbf{U}_i + \mathbf{J}_i^{-1}(\mathbf{R} - \boldsymbol{\theta}_i), \tag{7}$$

which is based on the Newton-Raphson method [31].

The Jacobean matrix $\mathbf{J}_i$ models the closed-loop galvanometer scanner, and it is automatically estimated. Among algorithms, the secant method is selected for the galvanometer scanner for fast and accurate learning [24]. In this case, $\mathbf{J}_i$ is a diagonal matrix, and its k-th element is updated by

$$j_{k,i} = \begin{cases} \frac{\theta_{k,i} - \theta_{k,i-1}}{u_{k,i} - u_{k,i-1}} & \text{for } |u_{k,i} - u_{k,i-1}| \geq \epsilon, \\ j_{k,i-1} & \text{otherwise,} \end{cases} \tag{8}$$

where $u_{k,i}$ and $\theta_{k,i}$ are the k-th element of $\mathbf{U}_i$ and $\boldsymbol{\theta}_i$, respectively, and ϵ is a threshold tuned to a small value at the implementation for stable learning.

After the input is updated by (7) and (8), $\mathbf{U}_{i+1}$ is converted to the time domain signal $u(t)$ for the next trial. As the initial condition of the learning, $\mathbf{J}_0$ and $\mathbf{U}_0$ are set to an identity matrix and $\mathbf{R}$, respectively. With the condition, the galvanometer scanner is regulated only by the feedback controller at $i = 0$ in order to collect data for the first learning iteration. For fast learning, the FPGA calculates the Fourier coefficient vectors in real time (cf. lock-in amplifiers), while the update laws (7) and (8) are implemented by the computer (Fig. 2(b)).

4.2. Experimental evaluation of learning effects

For the experimental validation of MF-IIC, the tracking error $e_x = r_\theta - \theta_x$ is measured at each trial, as shown in Fig. 7(a). MF-IIC quickly decreases a large error of 1.5 deg(rms) by a factor of 680 to 2.2 mdeg at $i = 20$. This experiment is repeated several times, and the tracking error converges in less than 10 s in all the cases. This fast learning is a benefit of the learning algorithm. Even if the bearing friction and the system model vary (e.g. due to the ambient temperature, the used period, or the maintenance), the fast and accurate scanning motion can be acquired onsite again in several seconds.

Fig. 7(b)(c) compares the time domain signals measured at $i = 0$ and 20. Without MF-IIC at $i = 0$, a large periodic tracking error of about ±2 degrees is clearly visible. This deterministic error is well-compensated by MF-IIC at $i = 20$ in Fig. 7(c). Consequently, MF-IIC enables the high-quality triangular motion at 125 Hz, as seen in Fig. 7(b).
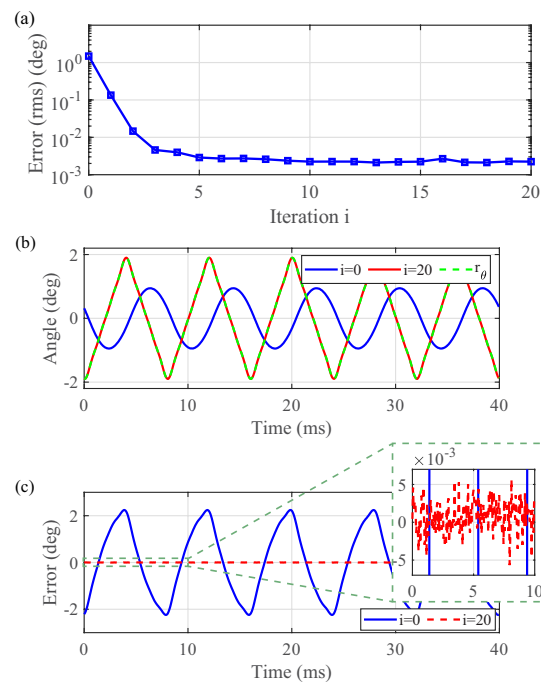

Fig. 7. Experimental results of MF-IIC: (a) the learning transient of the tracking error $e_x = r_\theta - \theta_x$, (b) the reference trajectory r_θ and the measured mirror angle θ_x at $i = 0$ and 20, and (c) the tracking error e_x at $i = 0$ and 20.

5. Image correction

Reconstructed 3-D images can be deformed, depending on the system configuration and the assembly tolerance of systems. Particularly in the case of the proposed configuration, the mirror angle θ_x extends the distance d_S to be measured by the confocal sensor. This results in scanning bow in an image. In order to correct the image distortion including the scanning bow, 3-D images are corrected based on a geometric model in this section.

5.1. Geometric model for image correction

Fig. 8 illustrates the proposed geometric model for the image correction. It is assumed that the confocal sensor and the stage with a calibration sample are sufficiently leveled off, which is relatively easy to satisfy by using a level or compass. Geometric parameters that are difficult to tune well are explicitly included in the model. They are the offset mirror angle θ_{off}, the offset of the reflection point on the mirror d_{off}. The symbol φ denotes the roll angle of the mirror, which is the angle at the center of the mirror R with respect to the calibration sample about the black dashed line in Fig. 8. The parameters L_1, L_2, L_3 are the distance between the sensor and the reflection point, between the sensor and the center of the mirror rotation, and between the sample surface and the reflection point, respectively. Note that d_{off}, θ_{off}, and φ result from the assembly and machining tolerances although they are desired to be zero.
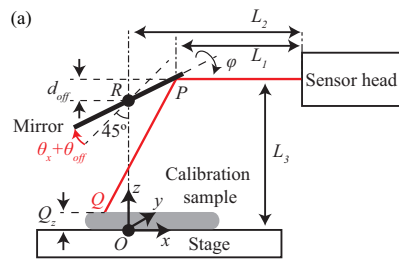

Fig. 8. Geometric model.

From Fig. 8, the distance measured by the confocal sensor d_S, which is the length of the red lines from the sensor head to the optical point Q in Fig. 8, is related to the geometric parameters by

$$d_S = L_2 - d_{off} \tan(\theta_x + \theta_{off} + 45°) + (L_3 - Q_z)\sqrt{1 + \tan^2 2(\theta_x + \theta_{off}) + \tan^2 2\varphi}, \quad (9)$$

where Q_z is the vertical position of the optical point Q on the sample and equivalent to the sample height.

If the parameters θ_{off}, d_{off}, L_2, L_3 and φ are estimated as $\hat{\theta}_{off}$, $\hat{d}_{off}$, $\hat{L}_2$, $\hat{L}_3$ and $\hat{\varphi}$, respectively, the sample height Q_z can be obtained from θ_x and d_S by rearranging (9) as follows:

$$Q_z = \hat{L}_3 + \frac{\hat{L}_2 - d_S - \hat{d}_{off} \tan(\theta_x + \hat{\theta}_{off} + 45°)}{\sqrt{1 + \tan^2 2(\theta_x + \hat{\theta}_{off}) + \tan^2 2\hat{\varphi}}}. \quad (10)$$

Similarly the lateral position Q_x of the optical point Q is given by

$$Q_x = \hat{d}_{off} \tan(\theta_x + \hat{\theta}_{off} + 45°) - (\hat{L}_3 - Q_z) \tan 2(\theta_x + \hat{\theta}_{off}). \quad (11)$$

In the above correction, Q_x depends on Q_z. Consequently, the data points cannot be assigned line by line to the pixel grid of an image. For simplicity of implementation, it is assumed that the variation of Q_z is sufficiently smaller than the scan range for an image, and the mean of Q_z is used as Q_z in (11).

5.2. Parameter estimation of geometric model

In order to utilize (10) and (11), the geometric parameters need to be well estimated. For this purpose, the mirror angle is changed between $\pm 2°$ with a step of $0.05°$, and the confocal sensor's

Table 1. Estimated geometric parameters.

Parameter	Value	Parameter	Value
$\hat{\theta}_{off}$,	-0.883°	$\hat{d}_{off}$,	-1.07 mm
$\hat{L}_2$	87.8 mm	$\hat{L}_3$	29.1 mm
$\hat{\varphi}$	4.94°	-	-

output is recorded at each angle. During the measurement, a silicon wafer with a thickness of 525 μm is selected as the calibration sample due to its flatness. This measurement is repeated by increasing the vertical sample position by 1 mm and 2 mm.

The five unknown parameters ($\theta_{off}, d_{off}, L_2, L_3$ and φ) are estimated by fitting the model (9) to the measured data sets simultaneously, as shown in Fig. 9(a). For the curve fitting, the MATLAB command *lsqcurvefit* is used such that the sum of the squared error between the measured and modeled d_S is minimized. The minimized squared error is 1526 μm^2. It corresponds to a root mean square (RMS) error of 2.5 μm, which is smaller than the accuracy of the confocal sensor. Table 1 lists the resulting estimated values.
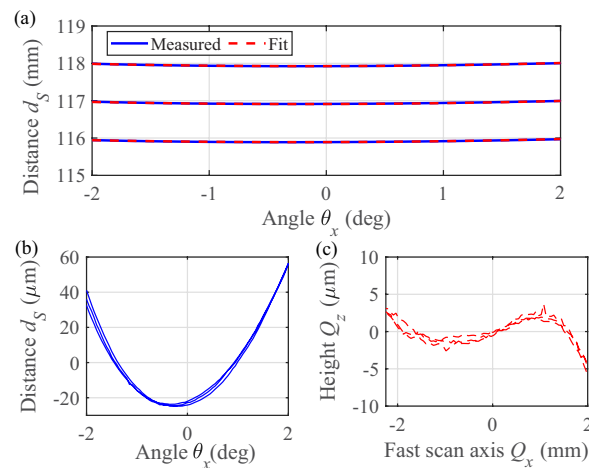

Fig. 9. Measured single line profiles for image correction and the result: (a) the distance d_S measured by the confocal sensor when a silicon wafer is scanned by changing the vertical sample position and the fit model (9), (b) the measured data without mean values, and (c) the corrected lines by (10) and (11) without mean values.

5.3. Evaluation of image correction

To evaluate the effectiveness of the image correction, the single line profiles measured in the previous section are corrected by (10) and (11) with the derived model, as shown in Fig. 9(b)(c), where the mean values of the data sets are removed for better linearity comparison.

The original single line profiles in Fig. 9(b) clearly show the scan bow. It varies the measured

distance 78 μm despite the flat sample. The large variation is successfully reduced to approximately $\pm 5\,\mu$m by the correction in Fig. 9(c). The residual error is no longer dominated by the scanning system geometry since it is close to the accuracy of the confocal sensor itself (7.5 μm). The effectiveness of the image correction is further confirmed by the 3-D imaging in the next section.

6. High-speed imaging

To demonstrate the proposed imaging system, samples are imaged by using the triangular motion in Sec. 4 for the galvanometer scanner and a constant speed motion at 4.5 mm/s for the linear stage. Fig. 10 shows a corner of a glass slide of a 1 mm thickness (cf. Fig. 3(c)). Without the image correction, the left and right sides of the image around $\pm 2°$ are slightly darker than the center due to the bowing effect in Fig. 10(a). Furthermore, the glass edges are deformed around $\pm 2°$. Note that white areas and dots in the image indicate pixels without measured data points, which can occur when the reflected intensity is too low. The image correction successfully eliminates the scan bow and the deformation in Fig. 10(b). An advantage of chromatic confocal displacement sensors is that they can measure the thickness of transparent materials. As a demonstration, Fig. 10(c) additionally shows the simultaneously measured thickness image.

To further demonstrate the effectiveness of the imaging system, a 10 euro cent coin in Fig. 11(a) is also imaged as shown in Fig. 11(b), which is corrected in Fig. 11(c). It is clearly visible that scan bow is well-corrected. In fact, the image correction makes the single line profile straight on a flat part of the coin. Note that the spikes around the texts are caused by the relatively low intensity of the reflected right due to the locally steep surface (cf. Section 3.1). Overall, the texts "Euro" on the coin are successfully reconstructed with the sharp contours without distortion.

The obtained images (Fig. 10 and Fig. 11) have 200×200 data points, and they are recorded at the sampling rate of 50 kHz. Consequently, images can be obtained at a frame rate of 1.25 fps. The scan range of the corrected images along the fast scan axis is 4 mm. Since the scanning frequency of the galvanometer scanner f_r is 125 Hz, the optical point scans the samples with one meter per second on average.

Fig. 12 shows the optical point position Q_x and velocity $\dot{Q}_x$ calculated from the measured mirror angle and (11). As discussed above, the optical point on the sample reaches the high speed of ± 1 m/s in a short cycle of 8 ms for the bidirectional scanning. The deceleration and acceleration time to reach 1 m/s from -1 m/s is 0.58 ms (Fig. 12), and the achieved acceleration is $3.4\,\text{km/s}^2$ (=350 g) on average. The high scanning speed and acceleration of the optical point can be realized since only the optical path is scanned, instead of the confocal sensor or the samples. When the confocal sensor is moved (Fig. 1(a)), its acceleration needs to be limited to $2\,\text{g}\,(=19.6\,\text{m/s}^2)$. The achievable maximum scanning speed with the acceleration time of 0.58 ms is ± 5.7 mm/s only. In other words, the proposed system can increase the scanning speed by a factor of 170 in comparison with the conventional configuration.

Overall, the proposed scanning system realizes the high optical scan speed of 1 m/s by accurately changing the optical path with the learning algorithm such that the commercial confocal displacement sensor obtains a 3-D image in 0.8 s only.

7. Conclusion and future work

For topography imaging of a surface, an off-the-shelf chromatic confocal displacement sensor is integrated, and its optical point is laterally scanned by a galvanometer scanner. While the proposed configuration changes the optical path for the fast scanning axis, it results in a scan bow and a tilted incident angle that decreases the intensity of the reflected light. Based on the experimental analysis, the scan range of the galvanometer scanner is set to $\pm 2°$ for fast imaging. The scan bow is well compensated by the model-based image correction. For the control of the galvanometer scanner, the low-bandwidth feedback controller is designed to eliminate a steady-state error, and MF-IIC is combined to decrease the tracking error by a factor of 680 for
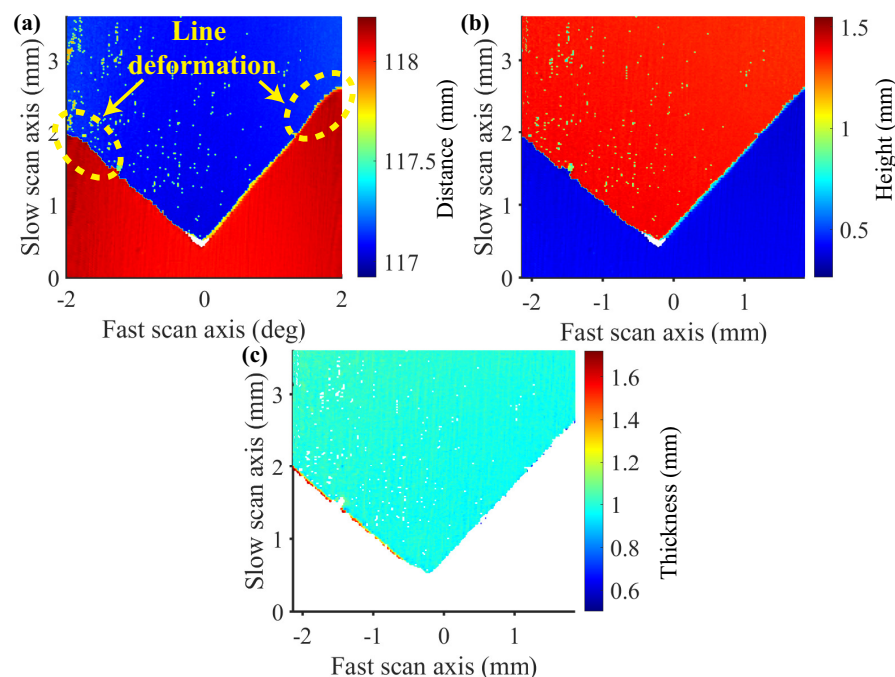
Fig. 10. Imaged glass slide corner: (a) original distance image, (b) corrected height image (c) corrected thickness image.

the 125 Hz triangular scanning motion. As a result, the optical point scans the surface at 1 m/s on average, such that topography and thickness images of 200×200 pixels are acquired for the frame rate of 1.25 fps. Future work includes the development of an imaging system with a 2-D scanning mirror for inline metrology.

Funding

Acknowledgments

Disclosures

The authors declare no additional conflicts of interest.
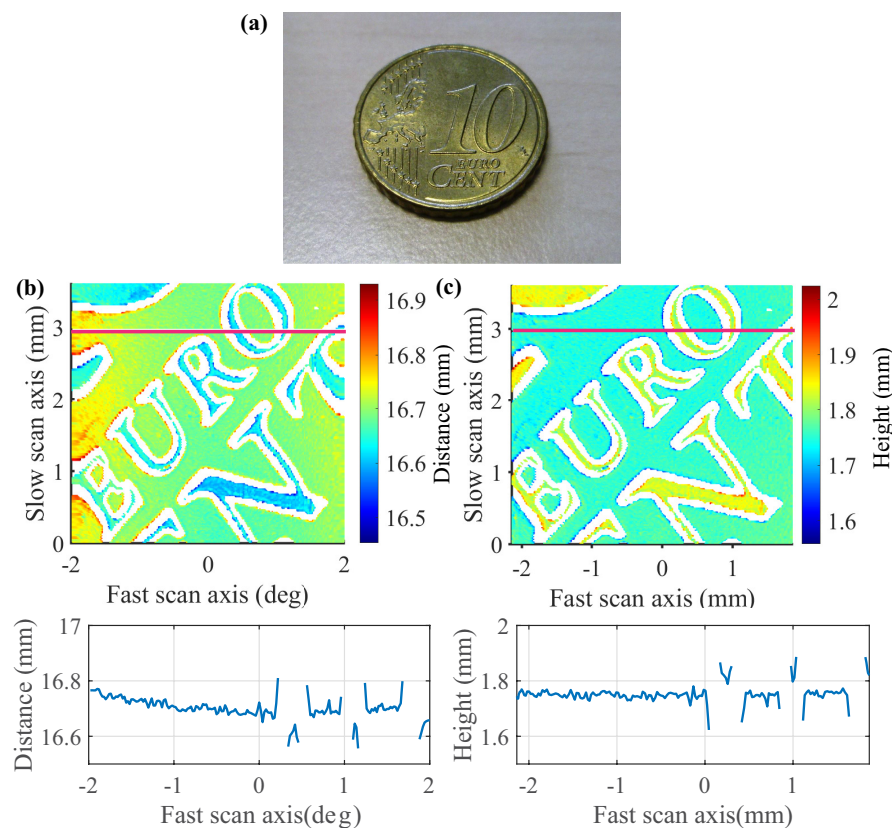
ACIN

Fig. 11. Ten euro cent coin: (a) a photograph and (b) original distance image of coin texts, and (c) corrected height image of the coin texts, where magenta lines represent the data sets for the single line profiles.

References

1. C. R. Garcia, R. C. Rumpf, H. H. Tsang, and J. H. Barton, "Effects of extreme surface roughness on 3d printed horn antenna," Electron. Lett. **49**, 734–736 (2013).
2. B. Pan, Y. Yang, and Y. Zhang, "Extraction of diamond grain topography from diamond tool surface using 3d surface measurement coupled with image analysis," Measurement **133**, 9–13 (2019).
3. R. Schmitt and F. Moenning, "Ensure success with inline-metrology," in *IMEKO XVIII World Congress,* (2006).
4. D.-H. Lee and N.-G. Cho, "Assessment of surface profile data acquired by a stylus profilometer," Meas. Sci. Technol. **23**, 105601 (2012).
5. F. Blais, "Review of 20 years of range sensor development," J. Electron. Imaging **13**, 231–240 (2004).
6. J. Schlarp, E. Csencsics, and G. Schitter, "Optical scanning of laser line sensors for 3D imaging," Appl. Opt. **57** (2018).
7. C. J. Weng, B. R. Lu, P. Y. Cheng, C. H. Hwang, and C. Y. Chen, "Measuring the thickness of transparent objects using a confocal displacement sensor," in *IEEE International Instrumentation and Measurement Technology Conference,* (2017), pp. 1–5.
8. T. Meinert, N. Weber, H. Zappe, and A. Seifert, "Varifocal MOEMS fiber scanner for confocal endomicroscopy," Opt. Express **22**, 31529–31544 (2014).
9. H. J. Jordan, "Optical chromatic confocal probes," in *XII International Colloquium on Surfaces,* (2008), pp. 200–209.
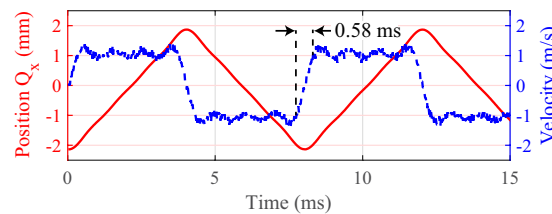
Fig. 12. Optical point position and velocity given by the measured mirror angle and (11).

10. Q. Cui and R. Liang, "Chromatic confocal microscopy using liquid crystal display panels," Appl. Opt. **58**, 2085–2090 (2019).
11. S. Cha, P. C. Lin, L. Zhu, P.-C. Sun, and Y. Fainman, "Nontranslational three-dimensional profilometry by chromatic confocal microscopy with dynamically configurable micromirror scanning," Appl. Opt. **39**, 2605–2613 (2000).
12. M. Hillenbrand, R. Weiss, C. Endrödy, A. Grewe, M. Hoffmann, and S. Sinzinger, "Chromatic confocal matrix sensor with actuated pinhole arrays," Appl. Opt. **54**, 4927–4936 (2015).
13. R. Leach, *Optical Measurement of Surface Topography* (Springer, 2011).
14. K. Tomlinson, C. T. Seagle, H. Huang, G. E. Smith, J. L. Taylor, and R. R. Paguio, "Enhanced dual confocal measurement system," Fusion Sci. Technol. **73**, 139–148 (2018).
15. S. Ito, J. Steininger, and G. Schitter, "Low-stiffness dual stage actuator for long rage positioning with nanometer resolution," Mechatronics **29**, 46–56 (2015).
16. K. M. Lynch, N. Marchuk, and M. L. Elwin, *Embedded Computing and Mechatronics with the PIC32 Microcontroller* (Newnes, 2015).
17. N. Vukašinović, D. Bračun, J. Možina, and J. Duhovnik, "The influence of incident angle, object colour and distance on cnc laser scanning," The Int. J. Adv. Manuf. Technol. **50**, 265–274 (2010).
18. R. P. Aylward, "Advanced galvanometerâĂŘbased optical scanner design," Sens. Rev. **23**, 216–222 (2003).
19. D. Matsuka, T. Tanaka, and M. Iwasaki, "Thermal demagnetization compensation for fast and precise positioning in galvanometer scanners," IEEE Transactions on Ind. Electron. **63**, 5514–5522 (2016).
20. H. W. Yoo, S. Ito, and G. Schitter, "High speed laser scanning microscopy by iterative learning control of a galvanometer scanner," Control. Eng. Pract. **50**, 12–21 (2016).
21. B. Armstrong-Hélouvry, P. Dupont, and C. Canudas de Wit, "A survey of models, analysis tools and compensation methods for the control of machines with friction," Automatica **30**, 1083 – 1138 (1994).
22. T. Hayakawa, T. Watanabe, T. Senoo, and M. Ishikawa, "Gain-compensated sinusoidal scanning of a galvanometer mirror in proportional-integral-differential control using the pre-emphasis technique for motion-blur compensation," Appl. Opt. **55**, 5640–5646 (2016).
23. Y. Li and J. Bechhoefer, "Model-free iterative control of repetitive dynamics for high-speed scanning in atomic force microscopy," Rev. Sci. Instruments **80**, 013702 (2009).
24. S. Ito, H. W. Yoo, and G. Schitter, "Comparison of modeling-free learning control algorithms for galvanometer scanner's periodic motion," in *IEEE International Conference on Advanced Intelligent Mechatronics,* (2017), pp. 1357–1362.
25. K. K. Leang, Q. Zou, and S. Devasia, "Feedforward control of piezoactuators in atomic force microscope systems," IEEE Control. Syst. Mag. **29**, 70–82 (2009).
26. D. A. Bristow, M. Tharayil, and A. G. Alleyne, "A survey of iterative learning control," IEEE Control. Syst. Mag. **26**, 96–114 (2006).
27. S. Ito, S. Troppmair, B. Lindner, F. Cigarini, and G. Schitter, "Long-range fast nanopositioner using nonlinearities of hybrid reluctance actuator for energy efficiency," IEEE Transactions on Ind. Electron. **66**, 3051–3059 (2019).
28. P. Louridas and C. Ebert, "Machine learning," IEEE Softw. **33**, 110–115 (2016).
29. S. Ito, H. W. Yoo, and G. Schitter, "Noise reduction of learning control for periodic motion of galvanometer scanner," in *IFAC World congress,* (2020).
30. V.-F. Duma, P. Tankam, J. Huang, J. Won, and J. P. Rolland, "Optimization of galvanometer scanning for optical coherence tomography," Appl. Opt. **54**, 5495–5507 (2015).
31. F. Cajori, "Historical note on the newton-raphson method of approximation," The Am. Math. Mon. **18**, 29–32 (1911).